Nanoscale Advances

ROYAL SOCIETY OF CHEMISTRY

PAPER

View Article Online
View Journal | View Issue

Cite this: *Nanoscale Adv.*, 2025, **7**, 2695

Microwave characterization of plasmonic antennas through electron energy loss spectroscopy†

Igor Getmanov, *[a] Qingxiao Wang,[b] Heng Wang,[a] Atif Shamim[a] and Dalaver H. Anjum [c]

The absence of suitable equipment has long hindered traditional microwave characterization of nano-antennas and their effective design at frequencies beyond several terahertz, limiting the exploration of the myriad applications of plasmonic antennas by the microwave engineering community and necessitating a paradigm shift in characterization methods. This work addresses this challenge by introducing a novel approach employing electron energy loss spectroscopy (EELS) to characterize input impedance and scattering parameters of plasmonic antennas from mid-infrared to optical frequencies. Central to this method is a newly developed theoretical framework that links electron energy loss probability with microwave scattering parameters, crucial for antenna design. We validated this approach through a study of a single plasmonic dipole, finding a good correspondence between the measured EEL spectra and our theoretical model, supported by our developed simulation model. Drawing upon this correlation, we proposed an algorithm for the reverse procedure of extracting *S*-parameters and input impedance from experimental EEL probability. Spatial profiles of input impedance and *S*-parameters for a single plasmonic dipole were experimentally characterized across the broad frequency spectrum ranging from 25 to 150 THz and compared with simulation results, revealing a robust correlation, particularly at resonant frequencies. Our non-contact method could serve as an alternative approach to microwave parameters characterization, functioning similarly to a vector network analyzer (VNA) but extending its capabilities to much higher frequencies, where VNAs are not available.

Received 19th November 2024
Accepted 19th March 2025

DOI: 10.1039/d4na00960f

rsc.li/nanoscale-advances

1 Introduction

Plasmonic antennas have proven effective for collecting and delivering free-space electromagnetic (EM) energy in a variety of applications, including sensing,[1,2] spectroscopy,[3–5] and energy harvesting.[6–9] Surface plasmon polaritons (SPPs), excited in metallic structures, offer substantial field enhancements and mode confinement beyond diffraction limits,[10,11] extensively utilized at optical frequencies[1,11,12] and now extending to mid-infrared[2,5–7,13] (MIR) and even terahertz (THz) frequencies.[3,14] Hot spot engineering for SPP modes can be employed to enhance the incident field through easily fabricated and integrated bowtie antennas, benefiting devices like metal–insulator–metal diodes.[6–8] The same strategy, applied to grid-based antenna design, improves wave absorption efficiency, paving the way for THz wave generation and infrared energy harvesting.[13,14] In addition, nonlinear effects induced by plasmonic high field enhancement can improve quantum dot radiation *via* the Purcell effect at optical frequencies.[15,16] Furthermore, near-field imaging techniques, such as scattering Scanning Near-field Optical Microscopy (s-SNOM), exploit naturally occurring plasmonic antennas formed by a conductive AFM tip in close proximity to the sample, enabling near-field spectroscopy and imaging.[17]

Given the promising applications of plasmonic antennas across a broad frequency spectrum from THz to optical frequencies, their experimental characterization is essential for effective antenna design. Traditional microwave characterization techniques, reliant on vector network analyzers and anechoic chambers, are typically utilized at radio frequencies but face limitations due to the lack of equipment beyond several THz.[14,18,19] Challenges also arise from probe parasitic effects starting from sub-THz frequencies[20] and the complete absence of RF probes at higher frequencies, making the conventional microwave characterization approach impractical. Consequently, researchers have begun to explore non-contact methods as alternative approaches for antenna characterization, moving beyond traditional microwave techniques.

Conventional far-field optical characterization methods, primarily relying on photo absorption spectroscopy commonly used in chemistry and semiconductor device analysis,[21–23] have

[a]*IMPACT Lab, King Abdullah University of Science and Technology, Thuwal 23955, Kingdom of Saudi Arabia. E-mail: igor.getmanov@kaust.edu.sa*

[b]*Imaging and Characterization Core Lab, King Abdullah University of Science and Technology, Thuwal 23955, Kingdom of Saudi Arabia*

[c]*Khalifa University, Abu Dhabi 127788, United Arab Emirates*

† Electronic supplementary information (ESI) available. See DOI: https://doi.org/10.1039/d4na00960f

been adapted for the study of plasmonic antennas of various types[24–27] and devices integrated with antennas.[25,28] While these methods serve well for resonance identification, they lack the capacity to provide valuable information on microwave parameters, such as input impedance, thereby falling short of fully characterizing the antenna performance. Researchers have turned their focus toward near-field characterization methods, including s-SNOM[29] and Electron Energy Loss Spectroscopy (EELS).[30] These techniques offer advantages over the mentioned far-field techniques by enabling up to sub-nanometer spatial resolution for near-field EM mode mapping in plasmonic antennas,[31–34] providing enhanced insights into SPP modes excited in antennas. While primary qualitative observations of various effects, including SPP wavelength confinement at antenna edges,[30,35] field enhancement,[36–38] and the loading effect on spatial mode distribution,[39] can be assessed, all these methods still lack the capability to provide comprehensive insights into essential microwave parameters, including *S*-parameters and input impedance, pivotal for effective antenna design.[40] It is noteworthy that recent attempts have been made to quantify the input impedance of folded dipole antennas by analyzing the SPP standing wave near-field measured in a transmission line through s-SNOM.[41,42] However, extending this approach to a broader range of antennas is restricted due to the strong dependence of near-field configuration on photon excitation conditions[31] and near-field disruption due to oblique wave incidence.[43]

In contrast, due to the localized excitation nature,[32,44] EELS circumvents the discussed limitations observed in s-SNOM for antenna near-field mapping. Existing approaches for interpreting the experimental EELS near-field signal of plasmonic antennas are traditionally linked to the Localized Density of States (LDOS),[32,35,36,45] although this interpretation remains a topic of debate.[46] Alternatively, some methods consider the EELS signal proportional to the induced electric field of the antenna.[47,48] However, such frameworks are scarcely applicable for the quantitative characterization of microwave parameters. Consequently, despite the development of various optical methodologies, conventional antenna design and its integration with other devices based on EELS characterization remains questionable due to a notable gap in interpreting the EEL spectra in terms of microwave parameters, such as *S*-parameters and input impedance. In this regard, despite its instrumentation advantages, EELS remains in its nascent stage concerning the microwave characterization of plasmonic antennas.

Therefore, in this study, we address this gap by introducing a novel theoretical framework bridging microwave scattering parameters and experimental EEL spectra. The electromagnetic nature of the electron loss, as postulated in our work, enables the establishment of the functional correlation between loss probability observed in EELS and microwave *S*-parameters. Furthermore, our framework involves the development of a simulation model capable of calculating scattering parameters under electron beam excitation conditions. Decent agreement observed between our theoretical model, which employs simulated *S*-parameters, and experimental EEL probability, as validated through EELS characterization of the fabricated plasmonic dipole, allows us, for the first time, to propose an algorithm for the reverse procedure of antenna input impedance and *S*-parameters characterization using experimental EEL probability. The frequency-dependent behavior and spatial distribution of the experimentally characterized *S*-parameters, which exhibit strong agreement with the simulation results at antenna resonance frequencies, highlight the effectiveness of our theoretical framework. This result, complemented by the exceptional spatial and frequency resolution offered by EELS, makes it a powerful tool for the microwave characterization of plasmonic antennas spanning from THz to optical frequencies.

2 Results and discussion

As previously discussed, before proceeding to the quantitative experimental characterization of *S*-parameters, it is essential to establish the theoretical background linking the experimental EEL spectra with these microwave characteristics. For this purpose, we initially analyze the conditions of the EELS experiment carried out in this study as they define the assumptions underlying our subsequently introduced theoretical framework.

Plasmonic antenna characterization can be performed through EELS, typically integrated with the Scanning Transmission Electron Microscope (STEM), as depicted by the simplified schematic in Fig. 1a. Within STEM EELS, the electron beam is generated and accelerated by the electron gun to achieve energy in the tens of kiloelectronvolts (keV). Following this, the electron beam is focused onto a sample by a series of electromagnetic lenses to form a probe of sub-nanometer diameter that defines the spatial resolution of the image. The electron probe interacts with the sample, resulting in the elastic and inelastic scattering of the electrons. These electrons are subsequently captured by the High-Angle Annular Dark Field (HAADF) detector and EEL spectrometer, enabling the recording of topographical and spectral images, respectively. The Spectral Image (SI) provides insight into the spatial distribution of spectra recorded at each electron probe excitation position and is found to be useful for element analysis,[49,50] band gap characterization,[51,52] and optical mode mapping.[32–35,47,48,53] To achieve the energy resolution of EEL spectra, defined by the zero-loss peak (ZLP) width,[54,55] sufficient for resolving the low-loss plasmonic resonances at energies down to tens of milli-electronvolts (meV), a monochromator is employed prior to focusing.

In the context of plasmonic antenna response to the electron beam excitation, the electron loses its energy through retardation by the self-induced electric field mediated through the antenna, thereby resulting in the fraction of the electrons that have lost the energy corresponding to plasmonic resonance $\hbar\omega_{spp}$, manifested as the resonance peak in the EEL spectrum. This reduction of electron-antenna interaction to its electromagnetic nature, known as classical formalism,[32,38,47] is incorporated in our microwave interpretation. We further assume that throughout the spectral image acquisition and beam scanning, the incident electron beam maintains a consistent state, implying energy resolution and probe size. This uniformity in the electron beam state across each pixel allows us to

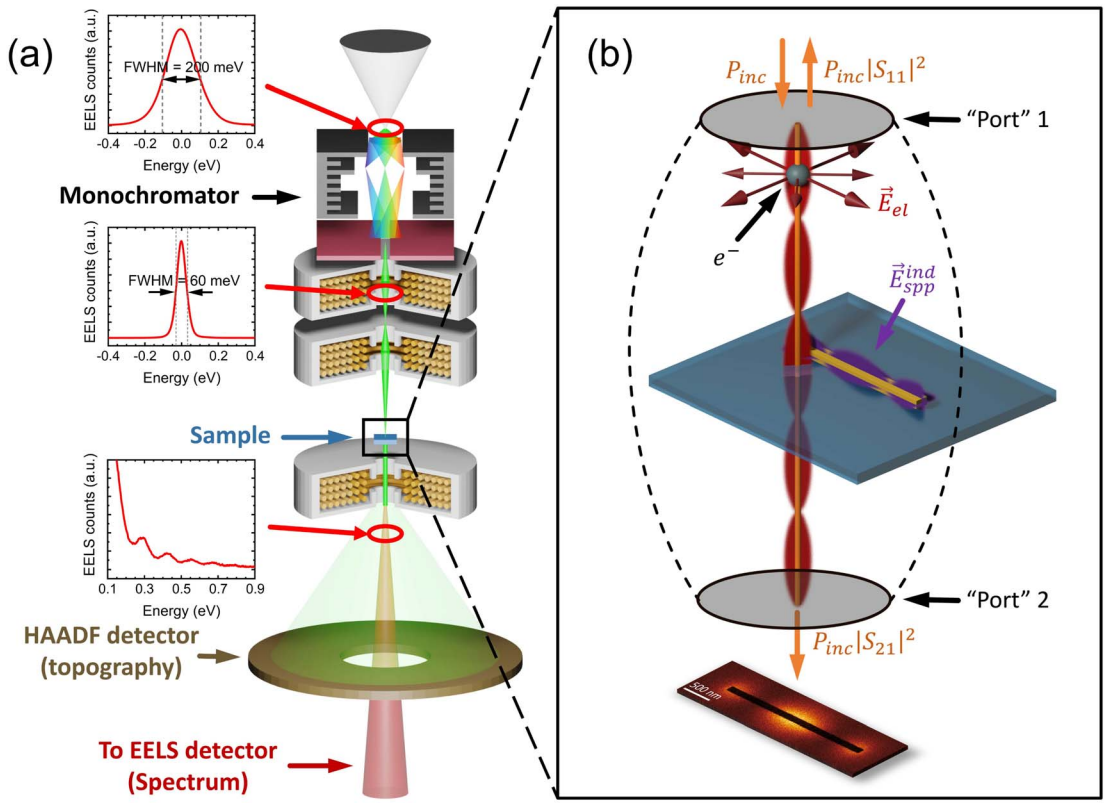

Fig. 1 Interpretation of the experiment within the context of electromagnetic wave losses: schematic of the experimental setup (a), featuring a Wien monochromator for achieving high energy resolution. The monochromator function is explained by the two ZLP peaks before and after the monochromation process shown in two inset figures. The energy losses resulting from the electron interaction with plasmonic antenna are captured by the spectral image acquisition, along with the topography image collected *via* the HAADF detector. Our approach (b), considering the electromagnetic nature of the interaction between the electron and the sample, is employed to analyze the observed energy losses in the experiment.

reduce our analysis to the immediate vicinity of the antenna. As schematically illustrated in Fig. 1b, this region is where the interaction between the electron and the near-field induced in the plasmonic antenna occurs.

2.1 Microwave interpretation of EEL spectrum

The microwave characterization of plasmonic antennas through the analysis of the experimental EEL spectra would be impossible without properly defining the connection between the microwave *S*-parameters and the EEL probability. In this section, we first establish this link through the theoretical interpretation of the electron energy loss induced by the plasmonic antenna from the perspective of microwave analysis.

With the abovementioned assumptions, the interaction between the electron beam and an antenna taking place in EELS experiment can be reduced to those provided by a single electron, represented for simplicity as a gray sphere in Fig. 1b. This approach has been extensively exploited in the literature.[32,36,38] We will follow a similar approach. Coulomb electric field of the electron moving along the z-axis with the velocity $\mathbf{v} = v_{el}\hat{z}$ has a continuous broadband spectral density $\mathbf{E}_{el}(\mathbf{r}, \omega)$. The classical analytical expressions of electric $\mathbf{E}_{el}(\mathbf{r}, \omega)$ and magnetic $\mathbf{H}_{el}(\mathbf{r}, \omega)$ fields in frequency domain are given as follows:[32]

$$\mathbf{E}_{el}(\mathbf{r},\omega) = 2\frac{kq_{el}\omega}{\gamma_L{}^2 v_{el}{}^2} e^{-i\frac{\omega}{v_{el}}z}\left[\gamma_L K_1\left(\frac{\omega}{v_{el}\gamma_L}R\right)\hat{R} + iK_0\left(\frac{\omega}{v_{el}\gamma_L}R\right)\hat{z}\right] \quad (1)$$

$$\mathbf{H}_{el}(\mathbf{r},\omega) = 2\frac{kq_{el}\omega}{\gamma_L v_{el}} e^{-i\frac{\omega}{v_{el}}z}\varepsilon_0 K_1\left(\frac{\omega}{v_{el}\gamma_L}R\right)\hat{\varphi} \quad (2)$$

Here $K_\nu(x)$ is the modified Bessel function of the second kind of ν-th order; ω is the angular frequency; R is the radial distance from the electron; $k = 1/4\pi\varepsilon_0$ is the Coulomb constant; q_{el} and v_{el} are the electron charge and velocity respectively; γ_L is the Lorentz contracting factor defining the field modification due to electron's relativistic speed. Although the spectral densities are broadband, the electric field is relatively localized in space, meaning that electron interaction will exponentially decay with a distance of $R = v_{el}\gamma_L/\omega$ from the electron position.[38,56] The orientation and distribution of the electric field, illustrating its confinement to the electrons' trajectory, are shown in Fig. 1b in red color. Moreover, the transversal field decay rate itself is a function of frequency, making the electromagnetic power density carried by the electron (P_{inc} in Fig. 1b) frequency dependent.

The verification that the fields in eqn (1) and (2) satisfy wave equations[38] serves to claim that the electron's fields can be regarded as an independent propagating field carrying power

along the electron's trajectory, as shown in Fig. 1b. Using these premises, the field associated with the moving electron, or electron beam, in frequency domain can be modeled as a propagating transverse magnetic (TM) mode,[10,57] sustained by a specific medium enclosed within a radially symmetric wire (depicted as an orange wire aligned with the electron's trajectory in Fig. 1b). Eventually, this mode interacts with both the plasmonic antenna field $\mathbf{E}_{\mathrm{spp}}^{\mathrm{ind}}$ and the support membrane in the aloof configuration, wherein the electron does not directly penetrate the metallic surface of the antenna. This interaction induces the dissipation of EM power carried by the electron, resulting in energy loss peaks at the resonant frequencies of the antenna.

In light of perspective on the electromagnetic interaction between the electron and antenna's SPP mode, we can formulate the probability density function through the total EM power lost by the electron as follows:[32,58]

$$\Delta E = \int_{-\infty}^{\infty} \mathrm{d}t P(t) = \int_{0}^{\infty} \mathrm{d}\omega \hbar\omega \frac{2}{\pi\hbar\omega} \int_{A} \langle \mathbf{S}_{\omega} \rangle \cdot \mathrm{d}\mathbf{A}' = \int_{0}^{\infty} \mathrm{d}\omega \hbar\omega \Gamma_{\mathrm{EEL}}(\omega) \tag{3}$$

with the EEL probability density function:

$$\Gamma_{\mathrm{EEL}}(\omega) = \frac{2}{\pi\hbar\omega} \int_{A} \langle \mathbf{S}_{\omega} \rangle \cdot \mathrm{d}\mathbf{A}' = \frac{2}{\pi\hbar\omega} P_{\mathrm{ext}}(\omega) \tag{4}$$

Here, $P(t)$ is the power lost by the electron at the time instant t due to SPP excitation in the antenna; $\langle \mathbf{S}_{\omega} \rangle$ is the averaged Poynting vector of the EM mode propagating along the electron's trajectory; $\mathrm{d}\mathbf{A}'$ is an element of the surface A enclosing the antenna and the electron beam (as indicated by the dashed curves in Fig. 1b); and $P_{\mathrm{ext}}(\omega) = P_{\mathrm{abs}} + P_{\mathrm{scat}}$ is the extinction power of the beam in frequency domain. The latter encompasses losses arising from both antenna scattering P_{scat} and the absorption P_{abs} (dissipation) losses of the SPP mode, as recently evidenced[59] in the analysis of localized plasmon scattering on circular dimers and other Cathodoluminescence (CL) experiments involving electron beam excitation of the antenna.[60,61] However, CL experiments specifically focus on scattering processes and fall beyond the scope of this work. This study is centered on integral losses, which encompass both scattering and absorption components.

The spatial integration in eqn (4) over the closed surface A encompassing the electron beam and antenna can be reduced to the elements surrounding the electron's EM mode, shown as shaded circles designated as Port 1 and Port 2 in Fig. 1b. Indeed, the losses contributed from considering lateral boundaries (dashed curves in Fig. 1b) are associated with the radiated CL field, which in regular EELS cannot be captured directly. From the microwave framework perspective, these two segments enclosing the beam before and after electron beam interaction with a plasmonic antenna can be regarded as inherent wave ports, where the EM mode carried by the electron beam is both excited and collected. The extinction power can be quantified as a power incident P_{inc} from the top of the sample, reduced by the back-reflected power (Port 1), and transmitted power through the sample captured at the bottom side (Port 2). This notation finds explanation through scattering parameters, commonly utilized by antenna designers and microwave engineers, as follows:

$$P_{\mathrm{ext}}(\omega) = P_{\mathrm{inc}}(\omega) \times (1 - |S_{11}|^2 - |S_{21}|^2) \tag{5}$$

Here, S_{11} and S_{21} represent the scattering parameters resulting from the beam interaction with the plasmonic antenna's SPP mode and the substrate underneath. Eqn (5) unfolds the contributions to power losses imposed on the electron beam wave. The first term denotes the incident power carried by the beam, while the second and third terms signify the reflected and transmitted power, respectively. The schematic representation of these contributions is depicted by orange arrows in Fig. 1b. Here we make a noteworthy remark that unlike the regular two-port microwave characterization, wherein EM feeding typically originates from the side of the sample, the electron beam passes through the substrate. This feeding configuration facilitates additional EM interaction with the substrate, thereby contributing to the overall reflection and absorption of the electron beam wave, irrespective of the antenna response. As a result, the scattering parameters S_{11} and S_{21} presented in eqn (5) incorporate contributions from both the antenna and the substrate background. Combining eqn (5) with (4), we get the ultimate relationship linking the probability density function, correlated with experimental EEL spectra, and scattering parameters:

$$\Gamma_{\mathrm{EEL}}(\omega) = \frac{2}{\pi\hbar\omega} P_{\mathrm{inc}}(\omega) \times \left(1 - |S_{11}|^2 - |S_{21}|^2\right) \tag{6}$$

with the spectral density of the EM power $P_{\mathrm{inc}}(\omega)$ carried by a single electron:

$$P_{\mathrm{inc}}(\omega) = \frac{2\pi}{2} \int_{R_{\mathrm{beam}}}^{\infty} \mathrm{Re}\left[\mathbf{E}_{\mathrm{el}} \times \mathbf{H}_{\mathrm{el}}^{*}\right]_z r \, \mathrm{d}r = -2\pi \frac{k^2 {q_{\mathrm{el}}}^2 \omega^2}{{v_{\mathrm{el}}}^3 {\gamma_{\mathrm{L}}}^2} \varepsilon_0 {R_{\mathrm{beam}}}^2 \times \left[{K_1}^2\left(\frac{\omega}{v_{\mathrm{el}}\gamma_{\mathrm{L}}} R_{\mathrm{beam}}\right) - K_0\left(\frac{\omega}{v_{\mathrm{el}}\gamma_{\mathrm{L}}} R_{\mathrm{beam}}\right) K_2\left(\frac{\omega}{v_{\mathrm{el}}\gamma_{\mathrm{L}}} R_{\mathrm{beam}}\right)\right] \tag{7}$$

Examination of eqn (7) reveals that the equation exhibits divergent behavior as the beam radius R_{beam} approaches zero, resulting in a singular EEL probability. This divergence stems from the inherent singularity of the EM field generated by a moving point charge [see eqn (1) and (2)]. However, as will be further discussed, this issue can be addressed by modeling the electron field as a plasmonic mode, sustained by a specific medium within a wire of small radius R_{beam}. By truncating the integration in eqn (7) at this finite wire radius, the singularity can be circumvented.

The simple relationship outlined in eqn (6) is a key result of this study, allowing us to correlate the microwave parameters with the EEL spectra and gain crucial insights into the main characteristics of plasmonic antennas embedded in scattering parameters. In comparison to other conventionally utilized methods for interpreting EEL spectra, such as LDOS[32,35,45] or effective polarizability,[32,36,38] our complimentary microwave approach summarized in eqn (6) holds the advantage of being

applicable for extracting *S*-parameters from the EEL signal, as we will expound upon in subsequent sections.

Despite its advantages, verification of eqn (6) through a comparison of the theoretical and experimental EEL spectra requires the estimation of the scattering parameters produced by antenna under specific localized electron beam excitation. For this purpose, a simulation model must be developed, a task that we address in the following section.

2.2 Simulation of scattering parameters under electron beam excitation conditions

The preliminary assessment of *S*-parameters generated by specific electron beam excitation for calculating theoretical EEL probability presents a challenge. In this section, we surmount this obstacle by introducing a comprehensive full-wave simulation model to calculate the scattering parameters of a plasmonic antenna under localized electron beam excitation.

Fig. 2a depicts the simulation model along with the spatial distribution of the electric field, demonstrating the successful excitation of a plasmonic dipole. The simulation has been carried out by solving the wave equation in frequency domain using COMSOL Multiphysics software. The model replicating the EELS experimental conditions consists of a gold plasmonic dipole with dimensions 2.58 μm × 100 nm × 35 nm, positioned on a silicon nitride substrate with a thickness t_{sub} = 100 nm. The dielectric properties of both gold and silicon nitride were taken from corresponding experimental data reported in the literature.[62,63] The excitation of the electron field TM-mode at Port 1, designated as the "source", is achieved by assigning specific dielectric properties to the electron beam confined within a plasmonic wire. Key parameters defining the beam's dielectric properties include the initial beam energy E_{beam}, governing the propagation constant, and the beam radius R_{beam}, determining the localization of the excitation (for electron beam properties calculation please refer to Section I and Fig. S1 of the ESI†). We select the following two values based on their optimal alignment with our experimental conditions: the beam radius equals half the pixel size (R_{beam} = 2.5 nm) of the SI, and the electron energy is set at 80 keV, which corresponds to our experimental conditions.

The electron beam field, with its transverse component distribution shown as a colormap in Fig. 2a, excites the plasmonic antenna through capacitive coupling, as evidenced by the discernible near-field distribution in the antenna plane. However, unlike conventional methodologies reported in the literature,[47,48] our approach, as outlined by eqn (6), prioritizes the analysis of antenna extinction power rather than focusing solely on the induced electric field. From the power analysis perspective, the lower wave port, labeled as the "detector", is utilized to capture the transmitted power $|S_{21}|^2$ through the sample, comprising the plasmonic antenna and dielectric support. The remaining power is either absorbed P_{abs}, scattered P_{scat} by the antenna, or reflected back towards the source port, quantified by a reflected power $|S_{11}|^2$.

The correctness of the electron beam mode excitation in the plasmonic wire was validated by comparing the analytical electron beam dispersion $\beta = \omega/v_{el}$[38,56,57] with the simulation results, shown as red dashed and black solid curves in Fig. 2b, respectively. Furthermore, a comparison of the radial field distribution for analytical and simulated solutions was performed for electric field components, as illustrated in Fig. 2c.

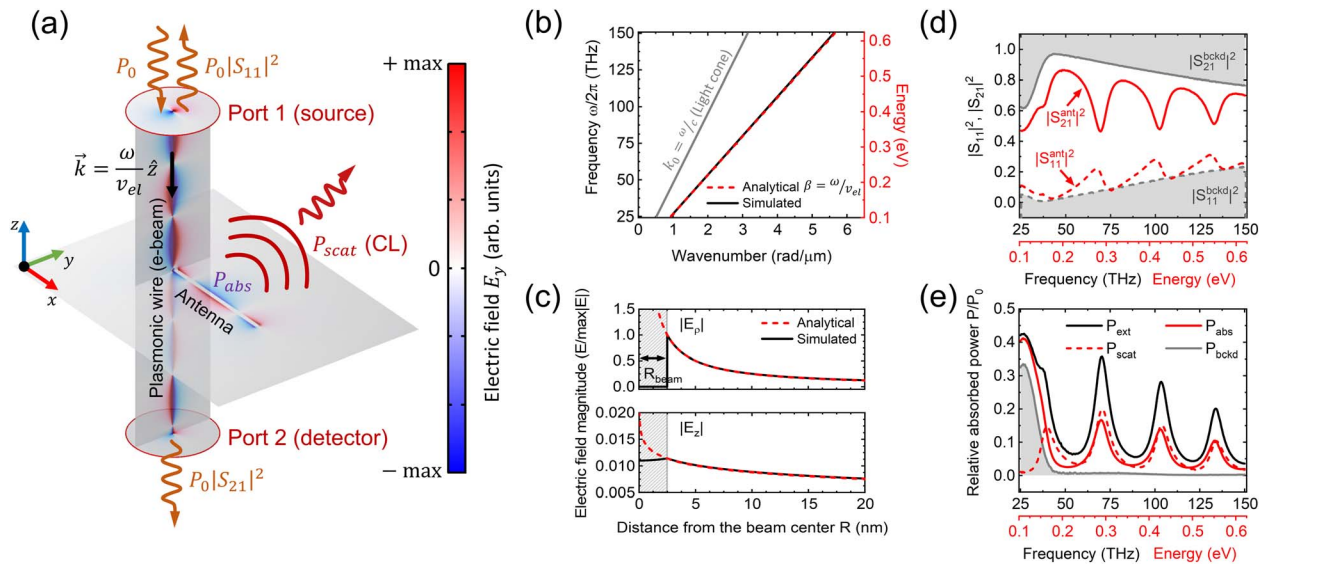

Fig. 2 Simulation procedure replicating EELS experiment: (a) full-wave simulation scheme featuring the results of the electric field in-plane component perpendicular to the antenna axis (E_y in this configuration) along with the depiction of the beam-antenna interaction with the subsequent loss mechanisms. The dispersion relationship (b) and electric field components (c) of the electron beam excited at Port 1 (black curves) and compared with the analytical solution (red dashed curves). The electromagnetic interaction between the simulated electron beam and the plasmonic dipole is characterized in terms of *S*-parameters (d). S_{11} and S_{21}, depicted in (d), are calculated at Port 1 and Port 2, respectively. The extinction power calculated through *S*-parameters (e) can be further decomposed into two contributions, namely, absorption losses (red solid curve) and scattering losses (red dashed curve).

Both cases exhibit a perfect correspondence, except for the electric field within the electron beam medium, which is outlined as a gray dashed region in Fig. 2c. The negligible radial field component inside the medium is attributed to charge screening defined by the properties of the plasmonic wire, aiding in averting singularities in a full-wave simulation. The electron field screening effect can be explained by the non-uniform distribution of electron density in the beam cross-section.[32,64] Given our focus on the aloof excitation of the plasmonic antenna by the electron beam, the interaction of the electron field with the SPP mode transpires outside the beam medium. Therefore, the simulated excitation can be regarded as being generated by the real electron.

The advantage of this model over other full-wave simulation-based approaches[38,48,65–67] lies in its capability to directly calculate the scattered parameters S_{11} and S_{21} for any resonant system. This versatility enables this method to provide the aloof excitation of various resonant modes of electromagnetic nature, not limited to plasmons, simultaneously providing the antenna engineers with valuable *S*-parameters for microwave characterization. Furthermore, this work marks the first instance where the *S*-parameters of a plasmonic antenna are evaluated through simulations under conditions inherent to electron beam excitation.

The results of the *S*-parameters calculated through the simulation model for a dipole plasmonic antenna with a length of $L_{dip} = 2.58$ μm, are shown in Fig. 2d. The extinction power, calculated using eqn (5), is also shown in Fig. 2e as a black curve, revealing four fundamental antenna resonances across range of 25 to 150 THz. Notably, these four resonances exhibit non-equidistant spacing, particularly at lower energies, attributed to the dispersion of the dielectric function $\varepsilon_{sub}(\omega)$ of the silicon nitride membrane.[62] In the simulation model shown in Fig. 2a, the plasmonic wire engages in electromagnetic interaction not only with the antenna but also with the background. This background interaction is indicated by an additional background slope in the reflection coefficient $|S_{11}^{bckd}|^2$, depicted by the dashed gray curve in Fig. 2d. The background *S*-parameters response shown in Fig. 2d is obtained by simulating the electron beam wave interaction with the silicon nitride in absence of any resonance structure. The monotonic increase of the background slope with rising frequency is attributed to the increase in the electrical length βt_{sub} of the electron beam as it traverses the dielectric of small constant thickness $t_{sub} = 100$ nm. This increase results in constructive interference in the reflections from two interfaces of the supportive membrane. Notably, this effect is predominantly independent of the antenna performance and should be excluded from the final spectra as a background.

We also would like to emphasize the mutual relationship between the contributions of the scattering and absorption losses to the overall extinction, as illustrated by the red curves in Fig. 2e. This is important for analyzing radiation efficiency from the perspective of antenna design. We can clearly see that the scattered power is of the same order as the absorbed power due to the plasmonic mode absorption. The only exception is for the first fundamental resonance, where the loss tangent $\tan\ \delta = \mathrm{Im}(\varepsilon_{sub})/\mathrm{Re}(\varepsilon_{sub})$ of the substrate is large,[62] resulting in high background losses P_{bckd} shown by gray shaded region.

In the preceding sections, we established the fundamental theoretical framework required for the subsequent introduction of the *S*-parameters extraction algorithm. By simulating both the extinction power and *S*-parameters under electron beam excitation, and applying the direct functional relationship between the EEL spectrum and microwave *S*-parameters as outlined in eqn (6), we can quantitatively evaluate the EEL probability for a plasmonic antenna. The next essential step is to validate this framework by comparing the theoretically derived spectrum with experimental EELS data, thereby demonstrating the feasibility of deriving the EEL spectrum from the *S*-parameters.

2.3 Verification of the microwave interpretation for EELS experiment

We now verify our proposed theoretical approach by conducting a comparative analysis between experimental EEL spectra and those derived using microwave interpretation. This verification will substantiate the feasibility of extracting the *S*-parameters from the experimental EEL probability function.

The plasmonic dipole with a length of $L_{dip} = 2.58$ μm, previously analyzed through simulations, where its resonances were observed as peaks in the extinction coefficient shown in Fig. 2e, was fabricated and experimentally characterized through EELS. The fabrication stack-up, including the dimensions of the plasmonic dipole and the supporting silicon nitride membrane, is illustrated in Fig. 3a. The STEM-acquired topography image of the fabricated dipole is presented in Fig. 3b.

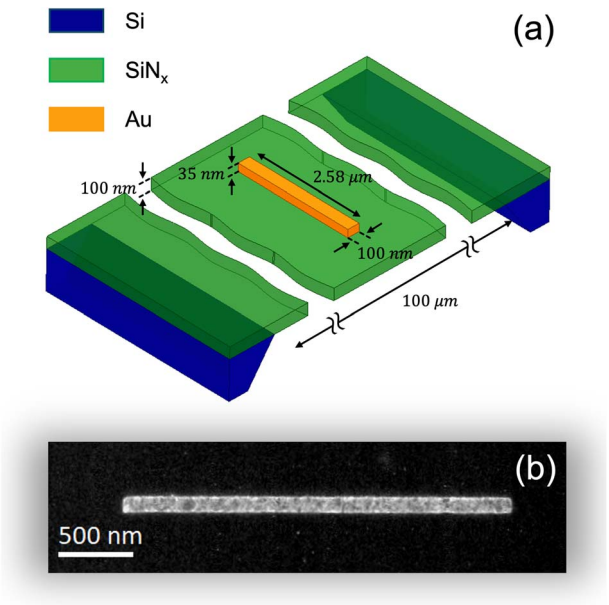

Fig. 3 Fabrication details of the plasmonic dipole antenna. (a) Schematic of the fabrication stack-up, showing the dipole dimensions (length = 2.58 μm, width = 100 μm, thickness = 35 nm) and the suspended membrane (100 μm × 100 μm, thickness = 100 nm) supported by a silicon substrate. (b) High-angle annular dark-field scanning transmission electron microscopy (HAADF-STEM) image of the fabricated plasmonic dipole.

Details regarding the fabrication procedure and EELS characterization conditions are provided in Methods section.

To address the non-uniform spatial distribution of experimentally observed spectra, characterized as standing wave patterns of LDOS along the dipole,[32,38,68] we select three distinct spectra obtained at the edge, intermediate, and central positions along the dipole axis, as depicted in Fig. 4a–c, respectively. Improvement of the signal-to-noise ratio in the experimental spectra (represented by the black solid curves) was achieved by averaging its response over a 16 × 16 pixel square, corresponding to a spatial uncertainty of ±40 nm in both directions in the antenna plane. The simulated spectra, presented as red dashed curves in Fig. 4a–c, were calculated using eqn (6), with the *S*-parameters evaluated *via* the above-mentioned simulation model for the identical experimental excitation positions illustrated in the inset. To account for the effect of EELS experimental resolution, the simulated spectra were subsequently convolved with the ZLP, following standard practice.[38,54,59]

Generally, there is a very good correlation between the simulated and experimental trends, with all resonance positions spanning from 25 to 150 THz (labeled as I–IV in Fig. 4a–c) showing strong agreement across all three spatial excitation points. This emphasizes the efficacy of result in eqn (6) in accurately interpreting the antenna SPP dispersion within the low-loss energy range through the evaluation of *S*-parameters. In particular, good correspondence between simulation and experiment is observed at the edge position (Fig. 4a). However, we observe a discrepancy between the experimental and simulated amplitudes of the EEL probability function when the electron beam feed departs from the dipole edge. This can be observed for resonances II and IV at the center position Fig. 4c and resonance III at the intermediate position (Fig. 4b), corresponding to their spatial resonance points in the spectral images shown to the left side of Fig. 4e. We refer such a disagreement to the differences in the simulated and experimental excitation conditions arising from the localization of the electron along its trajectory, as indicated by comparison of the left-side and central diagrams in Fig. 4d, respectively. On the contrary, a similar amplitude misfit is not observed at the edge position (Fig. 4a), which we attribute to the excitation not aligning precisely with the spatial resonance due to the virtual elongation of the dipole,[69,70] causing the SPP spatial resonance to extend slightly beyond the physical edge of the antenna. This rationale also explains the decrease in wavelength as the plasmonic wave approaches the abrupt truncation.[30,35]

The observed discrepancy in amplitudes of EEL spectra, as mentioned above, can be ascribed to the distinctiveness of the experimental electron excitation, which is characterized by its temporal and spatial localization in both transverse and longitudinal coordinates. As illustrated in the left-side diagram of Fig. 4d, prior to the interaction ($t = t_0$), the electron wave packet, appearing as a Gaussian shape, is localized in the upper plane. The spatial confinement persists after the interaction ($t = t_0 + t_{inter}$), with the electron retaining its localization along its

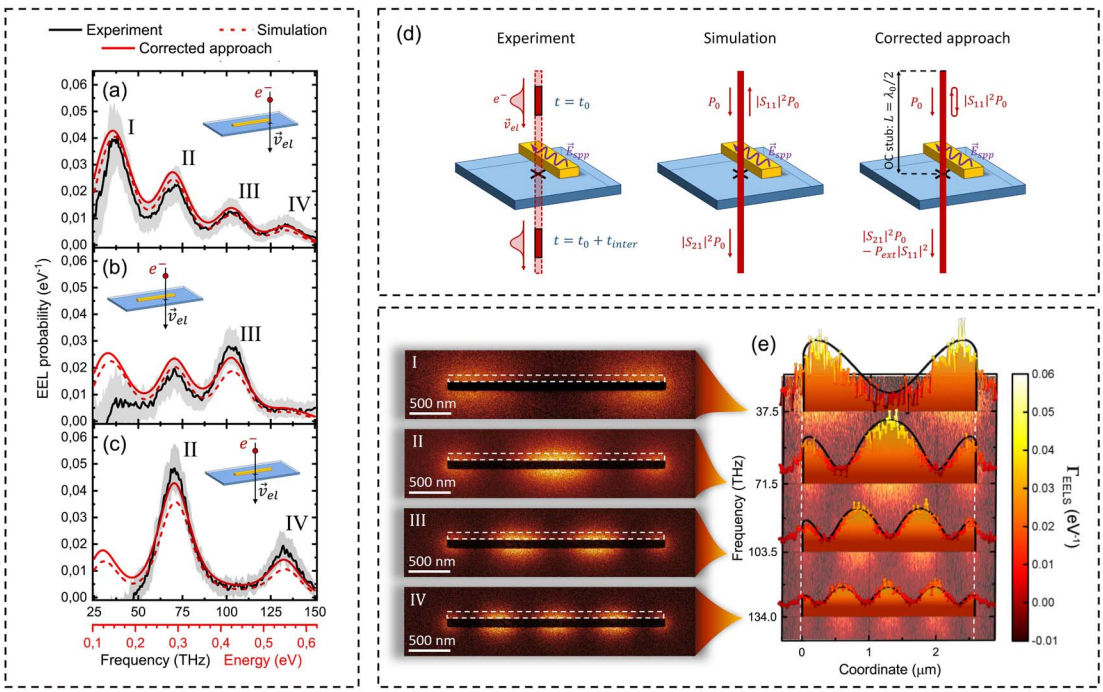

Fig. 4 Comparison between experimental spectra (black solid curve) obtained at the edge (a), intermediate (b), and central (c) positions along the dipole with aloof probe excitation (shown in the inset) at the distance 40 nm from the dipole, simulated spectra computed *via S*-parameters using eqn (6) (red dashed curve), and corrected approach (red solid curve) accounting for single electron excitation facilitated through the feedback scheme (d). The spatial distribution of EEL probabilities (e) along the dipole for all four resonances is presented as a color plot and contrasted with results from the corrected approach (black curves). Spectral images corresponding to all four resonances are displayed to the left of (e), with the region of profile acquisition outlined by a white dashed rectangle. The shaded areas in (a–c) demonstrate the standard deviation of the averaged spectra over 16 × 16 pixels.

trajectory despite experiencing energy loss equal to the plasmonic energy $\hbar\omega_{spp}$. A significant deviation becomes apparent when comparing the experimental and simulation diagrams: while the experimental setup demonstrates localized electron excitation, the simulation portrays a delocalized excitation along the electron trajectory. This discrepancy leads to an upward wave leakage, resulting in a reflected power characterized by the coefficient $|S_{11}|^2P_{inc}$, an observation of which in experiment may appear counterintuitive. This stems from the fact that the energy losses associated with the plasmonic energy excitation are significantly smaller than the primary energy of the electron beam $\hbar\omega_{spp} \ll E_0$ (*e.g.*, 0.2 eV $\ll$ 80 keV). Additionally, owing to the low current and the resulting large interelectron distance in the monochromated beam,[32,44] the electron-plasmonic interaction can be well described as localized along the electron trajectory, with electron longitudinal coordinates z varying at different time instances (Fig. 4d). This deviation from our introduced model, where the beam is assumed to be stationary and uniformly distributed along the electron trajectory, is apparent.

To compensate for this parasitic effect, corrections were implemented in the calculation of the extinction power in eqn (5), accounting for the localized electron interaction at different time intervals. In this adjustment, we assume that at the moment of interaction, the upper half-plane of the wire (corresponding to coordinates $z > z_{ant}$) no longer exists. As a result, the power that would typically be reflected as $|S_{11}|^2$ is redistributed between the transmitted power along the remaining lower part of the wire and the additional extinction power of the antenna. In summary, this correction implies the introduction of two virtual switching states for the electron beam, with its upper part "turning off" once the electron reaches the interaction region of the antenna to avert parasitic reflections. It is pertinent to emphasize that this corrected approach does not alter the simulation procedure outlined in the previous section. Rather, it utilizes the same simulation results but employs a corrected method for evaluating the extinction power.

From the perspective of frequency domain analysis, we performed such modifications by revising the calculation of the simulated extinction power, as illustrated in the central diagram in Fig. 4d. The reflected power calculated from the initial simulated results is redirected back to the sample utilizing the virtual feedback network (shown in the right-side picture in Fig. 4d), comprising an open-circuited $\lambda/2$ transmission line stub. This configuration ensures infinite impedance, mimicking the absence of a wire in the upper part. Subsequently, the redirected back reflected power interacts again with the antenna, resulting in an additional contribution to the extinction power $|S_{11}|^2P_{ext}$. This supplemental power combines with the initial extinction power P_{ext}, yielding a modified expression of the extinction power:

$$P_{ext}^{corr}(\omega) = P_{inc}(\omega)\frac{1-|S_{11}|^2-|S_{21}|^2}{1-|S_{11}|^2} \quad (8)$$

A more detailed derivation of the corrected extinction power in eqn (8) is provided in Section III of ESI.† The corrected EEL probability function, derived by substituting eqn (8) into the EM definition of the EEL probability from eqn (4), is shown in Fig. 4a–c. Notably, this corrected EEL probability (red solid curve) exhibits a considerably improved correlation with the experimental data compared to the uncorrected version. However, a significant deviation at frequencies <50 THz persists, which we attribute to the complementary excitation of a phonon mode in a silicon nitride dielectric slab[62] mediated by the antenna and not captured by the experiment due to the low signal-to-background ratio caused by the width of the ZLP. Furthermore, the simulated spatial distribution of the EEL probability along the antenna axis, represented by black curves in Fig. 4e for all four resonances, demonstrates remarkable alignment with the experimental data (colorful curve), emphasizing the effectiveness of our microwave approach. Importantly, these corrections do not alter the excitation conditions employed in our simulation model; rather, they only modify the extinction power calculation through eqn (8), which, as demonstrated further, will be applied to perform the reverse procedure of extracting *S*-parameters from the experimental EEL spectra.

2.4 Experimental scattering parameters extraction from EEL spectra

The robust correlation observed between the experimental and simulated EEL spectra, as discussed in the preceding section, enables the reverse procedure of extracting *S*-parameters from the acquired experimental EELS data. This approach, introduced below, unveils a novel technique for the microwave characterization of plasmonic antennas from mid-infrared to optical frequencies.

We developed an algorithm, depicted schematically in Fig. 5, designed to perform comprehensive microwave characterization of plasmonic antennas. This algorithm is capable of determining the distribution of antenna input impedance and *S*-parameters, akin to the model shown in Fig. 4d. The algorithm operates on input data consisting of the EEL probability function or, more generally, a spectral image containing the spatial distribution of the EEL spectrum across the sample. Subsequently, the algorithm transforms the EEL probability function into the extinction power spectra, a process made feasible by the established correlation between the simulated extinction power, described by eqn (8), and the experimental data. Following this step, the experimental signal can be effectively treated as deterministic within the microwave framework.

The input impedance is extracted from the experimentally obtained extinction power of the antenna using the transmission line model (depicted within the dashed area in Fig. 5), represented as a two-port network. This model serves to describe the EELS experiment *via* microwave circuit parameters. The characteristic impedances Z_0^{beam} and Z_0^{sub}, in this model represent the impedance of the TM-mode carried by the electron beam in vacuum and the dielectric substrate, respectively. The substrate here functions as the background, impacting the overall amplitudes of the *S*-parameters outlined in eqn (8), as discussed and illustrated through simulations in Fig. 2d. The

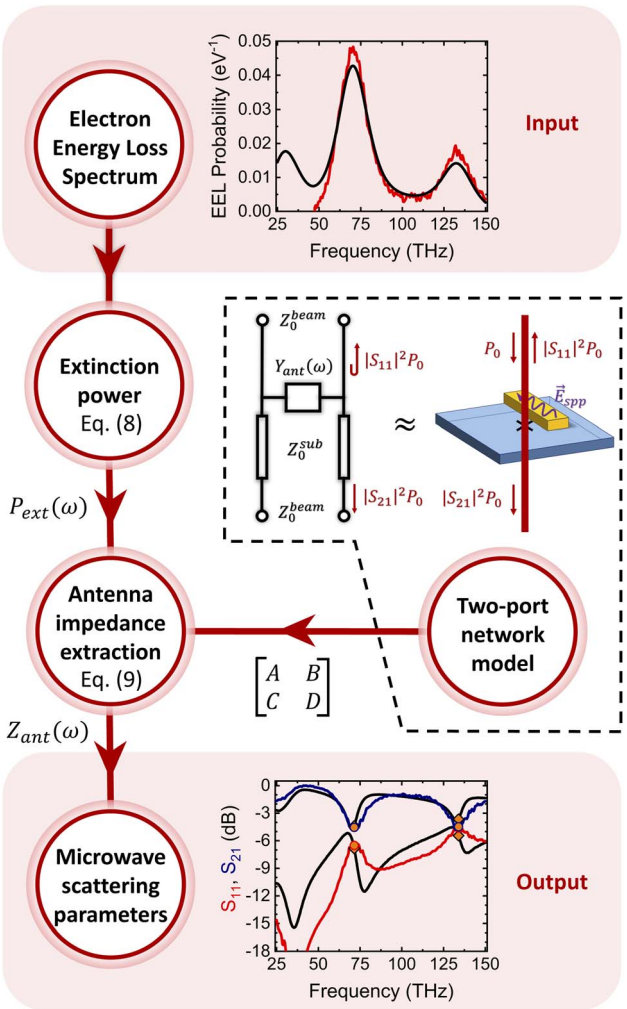

Fig. 5 Schematic representation of the algorithm for the extraction of microwave parameters, including input impedance $Z_{ant} = 1/Y_{ant}$, S_{11} and S_{21} parameters, from the electron energy loss probability Γ_{EEL}. At the core of the algorithm lies the microwave interpretation of plasmonic mode excitation in an antenna interacting with an electron beam. The interpretation is facilitated by the microwave model outlined in the dashed frame. Within this model, the relationship between the microwave parameters and the absorbed power of the beam can be established through ABCD-parameters, encompassing the electron beam interaction with both the background and the integrated antenna-substrate system. The inset plots are primarily illustrative, demonstrating the input (EEL probability) and output (*S*-parameters) functions of the algorithm, with comparisons between simulated data (black curves) and experimental results (colored curves).

extraction of S_{11} and S_{21} hereafter is performed for the entire sample, including both the antenna and the background. The latter is regarded as a transmission line with a length equal to the membrane thickness t_{sub}. The plasmonic antenna is represented as an admittance $Z_{ant} = 1/Y_{ant}$ connected in parallel to the beam transmission line traversing through the sample. It is noteworthy that the admittance encompasses the input impedance of the antenna and the capacitance formed by the gap between the antenna and the electron beam. This capacitive coupling induces a red shift in the resonance spectra observed in experiments when comparing near-field (electron) and far-field (plane wave) excitation of the dipole.[34,37,71]

Following the described model, the antenna admittance can be extracted from the extinction power using the following expression:

$$\mathrm{Re}\{Y_{ant}(\omega,\mathbf{R})\} = \frac{[P_{ext}(\omega,\mathbf{R}) + P_{bckd}(\omega)] \times \left[|\Delta|^2 P_{bckd}(\omega) + 4\right]}{4Z_0^{beam}|\xi|^2(1 - P_{ext}(\omega,\mathbf{R}) + P_{bckd}(\omega))} - \frac{|\Delta|^2 P_{bckd}(\omega)}{4Z_0^{beam}|\xi|^2(1 - P_{ext}(\omega,\mathbf{R}) + P_{bckd}(\omega))} \quad (9)$$

Here the parameters $\Delta = A + B/Z_0^{beam} + CZ_0^{beam} + D$ and $\xi = A + B/Z_0^{beam}$ are analytically derived using the microwave ABCD parameters of the background substrate,[72] considering the scenario where the antenna is absent ($Y_{ant} = 0$ in the transmission line model). These parameters depend on the supporting membrane thickness, beam propagation constant γ_{sub} in the dielectric, and characteristic impedances Z_0^{beam} and Z_0^{sub}. Eqn (9) has been derived through the analysis of the extinction power using the ABCD parameters of the microwave model depicted in Fig. 5 (see Section IV of ESI† for details). Similar to microwave measurements with a vector network analyzer (VNA), where *a priori* knowledge of the substrate is essential for calibration substrate design,[73,74] our algorithm similarly depends on the *a priori* knowledge of the dielectric properties of the background substrate, which we take from the literature.[62]

Analyzing eqn (9), it becomes evident that merely subtracting the background extinction power P_{bckd} from the power measured for the entire sample P_{ext}, which is already achieved by subtracting the ZLP from the raw EEL spectra and accounted for in the equation, will not entirely eliminate the background effect from the algorithm. Indeed, let us assume that there is no power absorption while the electron beam wave is traveling within the substrate, meaning $P_{bckd} = 0$ (this holds true at frequencies >rbin 50 THz, as has been demonstrated in Fig. 2e). In such a case, eqn (9) takes the following form:

$$\mathrm{Re}\{Y_{ant}(\omega,\mathbf{R})\} = \frac{1}{Z_0^{beam}} \frac{P_{ext}(\omega,\mathbf{R})}{|\xi|^2(1 - P_{ext}(\omega,\mathbf{R}))} \quad (10)$$

Analysis of eqn (10) reveals that even in the absence of substrate losses, the solution for the antenna admittance Y_{ant} is still influenced by substrate properties embedded in ξ in the denominator. As a result, simply excluding background absorbed power will not result in complete independence in antenna impedance calculation from the background.

As the antenna admittance is inherently complex, evaluating both its real and imaginary parts *via* eqn (9) introduces ambiguity. However, this ambiguity can be circumvented by considering solely the resonance frequencies of the EEL spectra, where the input impedance of the antenna becomes purely real. Under such conditions, eqn (9) offers an unambiguous method for characterizing the antenna's input impedance through experimental EELS data.

We demonstrate the efficiency of our algorithm by extracting the input impedance of a plasmonic antenna, as shown in Fig. 6a and b, from the experimental EEL spectra obtained at two distinct coordinates: the edge (Fig. 4a) and the center (Fig. 4c) of the plasmonic dipole. The input impedance is normalized to the characteristic impedance of the electron beam ($Z_0^{\text{beam}} = 675\ \Omega$), which was derived from simulations, to estimate the matching effect between the antenna and the beam. To account for the energy spread induced by the ZLP convolution with the true antenna response, we performed additional calibration of the EEL spectra prior to executing the algorithm by applying a correction factor to define the resonance amplitude decrease. The calibration curve was obtained by analyzing the dynamics of resonance peaks amplitudes with varying ZLP widths (see Section V of ESI† for details). Comparing the simulated (black solid curve) input impedance results with those extracted from both simulated (red curve) and experimental (blue curve) EEL probability functions using eqn (9), it is evident that at the resonance frequencies (identified by orange markers), the deviation between the theoretical predictions and the output of the algorithm is minimal. This observation indicates that our algorithm performs most effectively at resonance frequencies. The discrepancies observed between the experimentally characterized and simulated input impedances at non-resonance frequencies can be attributed to the significant imaginary component of the antenna impedance Z_{ant} (see Fig. S4 in ESI†), which our algorithm does not account for, prioritizing the reduction of ambiguity.

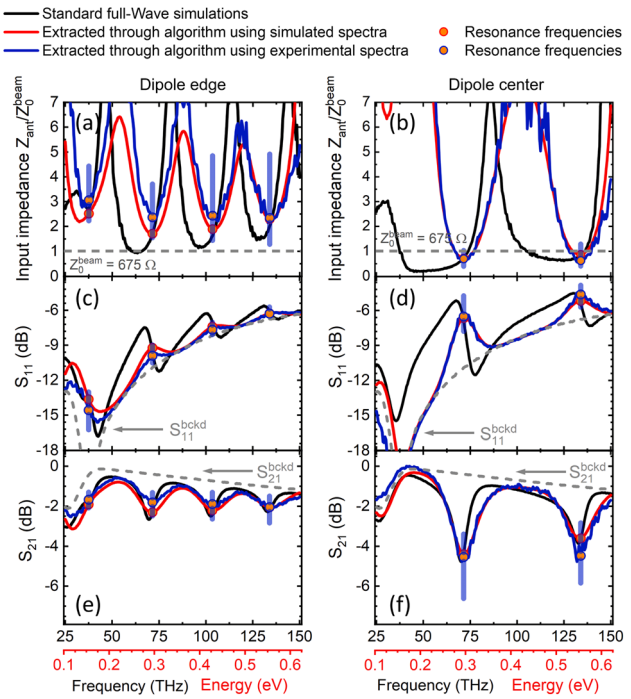

Fig. 6 Microwave parameters derived *via* our algorithm utilizing experimental EEL spectra (blue curve) acquired at the edge (left column) and center (right column) of the plasmonic dipole in an aloof configuration: input impedance Z_{ant} (a and b) relative to the characteristic impedance of the beam Z_0^{beam}, reflection S_{11} (c and d), and transmission S_{21} (e and f) coefficients of the electron beam traversing the sample. In comparison, the simulated microwave parameters and those obtained through our algorithm with simulated EEL probabilities are presented as black solid and red curves, respectively. The orange markers correspond to the EELS resonance peaks identified as points of minimal uncertainty of the algorithm. Blue shaded bars represent the error in the extracted parameters at resonances, calculated using the standard deviation from averaging 16 × 16 pixel segments of the experimental spectra (refer to Fig. 4a and c.).

In the final stage, the algorithm utilizes the transmission line model, incorporating the already determined antenna admittance Y_{ant}, to calculate the scattering parameters. According to our model, the reference planes of the two-port network, used to determine the *S*-parameters, are positioned immediately before and after the sample, comprising the antenna and the membrane. The S_{11} and S_{21} parameters, calculated from the experimentally characterized input impedance, are depicted in Fig. 6c–f for the edge and center excitations, respectively. The numerical values of the three extracted microwave parameters at the resonance frequencies, which are presented in Table 1, exhibit a good agreement with the simulated results obtained through beam excitation. This agreement is particularly notable for the *S*-parameters. The comprehensive quantitative results of the algorithm, illustrated in Fig. 6, signify a groundbreaking contribution to traditional microwave antenna characterization at mid-infrared frequencies. This advancement establishes EELS as a viable alternative to the vector network analyzer, which is non-existent at such high frequencies, thereby paving the way for conventional plasmonic antenna design.

The input impedance and scattering parameters depicted in Fig. 6 are fundamental microwave characteristics essential for antenna design, offering invaluable insights into the operation of plasmonic antennas from a microwave perspective. The resonance frequencies observed in the EEL spectra at both the edge and center coincide with an increase in S_{11} and a significant reduction in S_{21} relative to their background values (as represented by gray dashed curves in Fig. 6c and f). This response can be analyzed through the two-port network analysis, where the incoming power is distributed along two pathways: one through the transmission line traversing through the substrate towards the second port (EELS detector) and the other through the antenna. The power absorbed by the antenna can be described as follows:

$$P_{\text{ext}}^{\text{ant}}(Z_{\text{ant}}) = P_{\text{inc}}|1 + S_{11}(Z_{\text{ant}})|^2 \text{Re}\left\{\frac{Z_0^{\text{beam}}}{Z_{\text{ant}}}\right\} \quad (11)$$

Here, we discern two factors influencing the power absorbed by the antenna. Firstly, the relative input impedance of the antenna $Z_{\text{ant}}/Z_0^{\text{beam}}$ should decrease as it approaches the EELS resonance in order to satisfy the enhancement of the power in eqn (11) absorbed by the antenna. This trend is observed in the experimentally characterized input impedances at resonance frequencies in Fig. 6a and c. In addition, we notice that the input impedances characterized at the center position along the antenna are lower compared to those at the edge, resulting in an increased extinction power P_{ext} and, consequently, higher amplitude of the EEL spectra (compare resonances II and IV in

Table 1 Experimentally extracted and simulated microwave parameters at resonance frequencies

		Simulated			Experimental		
Resonance	Frequency (THz)	Z_{in}/Z_0^{beam}	S_{11} (dB)	S_{21} (dB)	Z_{in}/Z_0^{beam}	S_{11} (dB)	S_{21} (dB)
I (edge)	37.5	2.75	−13.74	−1.75	3.05 ± 1.10	−14.57 ± 1.62	−1.67 ± 0.39
II (edge)	71.5	1.68	−9.533	−2.29	2.37 ± 1.07	−9.89 ± 0.77	−1.81 ± 0.59
III (edge)	103.5	1.62	−7.01	−2.44	2.44 ± 1.7	−7.66 ± 0.53	−1.89 ± 0.67
IV (edge)	134.0	2.03	−6.12	−2.20	2.34 ± 1.82	−6.29 ± 0.48	−2.04 ± 0.67
II (center)	71.5	0.73	−6.85	−4.54	0.70 ± 0.31	−6.51 ± 1.53	−3.65 ± 1.61
IV (center)	134.0	0.84	−5.45	−3.65	0.62 ± 0.44	−4.62 ± 0.93	−4.48 ± 1.50

Fig. 4a and c, respectively). Simultaneously, the reflection coefficient S_{11} is also influenced by the antenna input impedance, with the lower impedance values leading to an increase in S_{11}, as evidenced by the peaks observed in Fig. 6c and d. In this context, improving impedance matching to minimize the S_{11} magnitude would make the antenna input impedance Z_{ant} infinite, thereby reducing the entire two-port network to the background scenario. This behavior extends to non-resonance frequencies, where the significant imaginary part of the input impedance does not contribute to absorption power.

It was demonstrated that our algorithm exhibits the least uncertainty at resonance frequencies, where the antenna input impedance is real. Additionally, it is evident that the microwave parameters are expected to vary with the excitation coordinate along the antenna, reflecting the spatial dependence of the EEL probability (Fig. 4e). By applying our algorithm to each pixel of the experimental spectral image, we can characterize the spatial distribution of the microwave parameters, providing comprehensive insights into antenna behavior. This capability, facilitated by the non-contact EELS technique, allows for the achievement of complete characterization with just one spectral image acquisition, offering advantage over traditional vector network analyzers. This advantageous feature can be applied, for instance, to determine the optimal spatial integration of the antenna with the device, thereby achieving improved matching.[6,9]

The spatial distribution of input impedance and scattering parameters at four fundamental resonance frequencies along the dipole in aloof configuration (at the same excitation positions as indicated by white dashed frames in the spectral images under Fig. 4e) were characterized using our extraction algorithm, as demonstrated in Fig. 7a–c. Comparison with

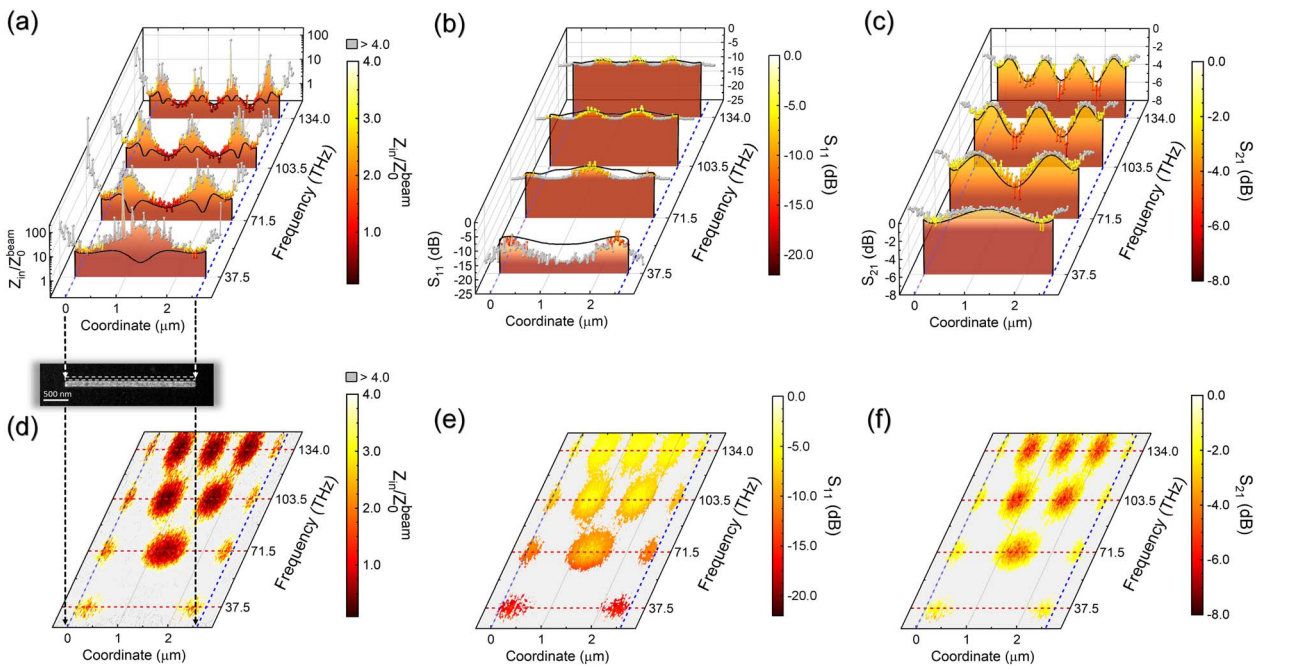

Fig. 7 The profiles of experimentally characterized microwave parameters (color plots) at the first four resonances of the plasmonic dipole: input impedance Z_{in} (a) relative to the beam characteristic impedance Z_0^{beam}, S_{11} (b), and S_{21} (c) parameters. The microwave parameters obtained through full-wave simulations are shown alongside as black curves. Regions of considerable discrepancy between experimentally characterized and simulated impedances are depicted as gray points in (a–c), assisting in identifying areas with minimal uncertainty, illustrated as color spots in the maps (d–f) for the above-shown parameters. The arrows denote the positions of the edges of the investigated dipole. The dashed area in the dipole topography image (shown below (a)) highlights the region from which the microwave parameter profiles were extracted.

corresponding simulated microwave parameters (shown as black curves) reveals a strong correlation at spatial resonances, defined as regions of high EELS signal intensities in the spectral images (compare Fig. 4e with the results in Fig. 7a–c).

On the other hand, the input impedance significantly deviates from simulated values at non-resonant points, as depicted in gray in Fig. 7a, due to the reasons analogous to those discussed earlier in the spectral response analysis. Furthermore, at these non-resonant spatial coordinates, the input impedance can exceed the electron characteristic impedance Z_0^{beam} by roughly tenfold. From a microwave perspective, such high impedance resembles an open-circuit in the two-port network, resulting in a background EEL spectrum devoid of meaningful signal from the plasmonic antenna. In this sense, we can establish a criterion for minimal uncertainty in spatial microwave parameters characterization, stipulating that only spatial coordinates where the input impedance $Z_{\text{ant}} < 4Z_0^{\text{beam}}$, which corresponds to the error in $|S_{11}| \leq -3$ dB, should be considered reliable. This threshold approximately delineates the EEL spectrum corresponding to the background signal. With these constraints, we conduct spatial mapping of the input impedance and scattering parameters S_{11} and S_{21}, as represented in Fig. 7d–f, respectively, illustrating their dynamics along the plasmonic dipole. In these maps, we discern that only the localized regions, centered around spatial resonances, genuinely identify the areas of minimal uncertainty in the microwave parameters characterization. However, we clearly see that even when considering the points of least certainty, the transmission coefficient S_{21} matches perfectly with simulations along all the spatial profiles (Fig. 7c), also capturing the variation of the peak intensity along the dipole identifying the wavelength compression effect,[30,35] when approaching the edge.

Quantitative spatial mapping of microwave parameters can play a pivotal role in understanding the characteristics of the antenna. Thus, at all spatial resonances, the antenna input impedance value closely matches with the beam characteristic impedance $Z_0^{\text{beam}} = 675\ \Omega$, as captured by the map in Fig. 7d. This result indicates the occurrence of "open-circuit" resonance along the plasmonic dipole,[41] where the current is minimized, leading to significantly higher input impedance compared to the standard 50 Ω port impedance typically utilized in microwave characterization. Consequently, voltage reaches its maximum at these coordinates, resulting in electric field enhancement around the dipole.[36,38] This observation demonstrates a correlation between the scattering parameters and the near-field of the antenna, which exhibit similar spatial distribution.[30]

3 Conclusions

This study presents a novel application of Electron Energy Loss Spectroscopy for the microwave characterization of input impedance and *S*-parameters in plasmonic antennas over a broad frequency range, from mid-infrared to optical frequencies. We have developed the comprehensive theoretical framework to establish the functional relationship between the experimental EEL probability and microwave scattering parameters *via* the extinction of electromagnetic power carried by the electron beam. The strong correlation observed between experimental spectra and those derived from simulated *S*-parameters, evident across a broad frequency range and various localized excitation positions, as exemplified by the plasmonic dipole case, proved possible the development of a reverse algorithm. This algorithm performs the extraction of *S*-parameters from the experimental EEL probability by utilizing a two-port network representation of the EELS experiment. The efficacy of the proposed method has been demonstrated through the characterization of input impedance and *S*-parameters frequency response, along with their spatial distribution for the plasmonic dipole. Through comparative analysis of experimental and simulated results, we established the constraints defining points of minimal uncertainty in microwave characterization across spatial and frequency domains. Furthermore, this study delves into the physical insights gleaned from the quantitative characterization of the plasmonic dipole through EELS, highlighting the value and utility of the developed method. Establishing a solid link between the microwave parameters and EEL probability offers promising prospects for utilizing EELS as an alternative to a vector network analyzer, which is not available at mid-infrared to optical frequency range. We believe that this contribution holds great promise for antenna engineers focusing on providing reliable plasmonic antenna solutions at such high frequencies.

4 Methods

4.1 Sample fabrication

The electron beam lithography and lift-off process has been adopted from[33] to fabricate the dipole. The plasmonic dipole was fabricated on commercially available TEM silicon nitride membrane with a thickness of 100 nm (TED Pella, Inc.). AR-P 6200.04 resist (Allresist GmbH) was spin-coated onto the silicon nitride membrane at 6000 rpm for 60 seconds and baked for 3 minutes at 150 °C to achieve a resist thickness of around 80 nm. Subsequently, the plasmonic dipole pattern was exposed using a Crestec CABL 9000C electron beam lithography system. The exposed sample was developed using AR 600-546 developer for 1 minute, followed by treatment with Oxylene and Isopropanol for 5 and 30 seconds, respectively. Following development, a 5/35 nm layers of Ti/Au were deposited using the e-beam evaporation technique. The lift-off was performed using AR 600-71 resist remover. Schematics of all fabrication steps are provided in Fig. S2 of ESI.†

4.2 STEM-EELS characterization

The fabricated dipole was characterized using FEI Themis Z microscope operating at 80 kV in STEM mode. To achieve high energy resolution, a Wien monochromator was employed, with its excitation voltage optimized to achieve a FWHM of the ZLP of 60 meV (Fig. 1a). Spectra acquisition was carried out in a microprobe configuration, where spherical aberrations were compensated through the Cs correction. The SI was acquired around the plasmonic dipole with a step size of 5 nm and

a dwell time of 6 milliseconds. EELS spectra were recorded using a Gatan K3 energy filtered camera with a dispersion of 0.003 eV per channel.

Data availability

The code for converting EEL spectra to microwave parameters can be found at **https://github.com/inghades/MiCharEL_Matlab** with **https://doi.org/10.5281/zenodo.15000562**. The version of the code employed for this study is version 1.0.

Author contributions

Igor Getmanov and Atif Shamim conceived and designed the study. Igor Getmanov developed the theoretical framework and simulation model, designed the plasmonic antenna, and created the algorithm for extracting microwave parameters from EEL spectra. Qingxiao Wang, Dalaver Anjum and Igor Getmanov carried out experimental characterization of the plasmonic antenna using EELS and analyzed the data. Heng Wang and Igor Getmanov fabricated the plasmonic antenna on a TEM aperture. Igor Getmanov and Atif Shamim wrote the manuscript.

Conflicts of interest

There are no conflicts to declare.

Acknowledgements

The authors thank Camelia Florica for assisting with the fabrication of plasmonic antennas. We express our appreciation to the staff of the KAUST Nanofabrication and Imaging and Characterization Core Labs for providing the necessary technical assistance.

Notes and references

1 N. Liu, M. L. Tang, M. Hentschel, H. Giessen and A. P. Alivisatos, *Nat. Mater.*, 2011, **10**, 631–636.
2 X. C. Tan, H. Zhang, J. Y. Li, H. W. Wan, Q. S. Guo, H. B. Zhu, H. Liu and F. Yi, *Nat. Commun.*, 2020, **11**, 5245.
3 K. Weber, M. L. Nesterov, T. Weiss, M. Scherer, M. Hentschel, J. Vogt, C. Huck, W. W. Li, M. Dressel, H. Giessen and F. Neubrech, *ACS Photonics*, 2017, **4**, 45–51.
4 R. Adato and H. Altug, *Nat. Commun.*, 2013, **4**, 2154.
5 H. Aouani, H. Sipova, M. Rahmani, M. Navarro-Cia, K. Hegnerova, J. Homola, M. Hong and S. A. Maier, *ACS Nano*, 2013, **7**, 669–675.
6 M. N. Gadalla, M. Abdel-Rahman and A. Shamim, *Sci. Rep.*, 2014, **4**, 4270.
7 G. Jayaswal, A. Belkadi, A. Meredov, B. Pelz, G. Moddel and A. Shamim, *Mater. Today Energy*, 2018, **7**, 1–9.
8 A. Weerakkody, A. Belkadi and G. Moddel, *ACS Appl. Nano Mater.*, 2021, **4**, 2470–2475.
9 A. Belkadi, A. Weerakkody, G. Lasser and G. Moddel, *ACS Photonics*, 2023, **10**, 3866–3874.
10 S. A. Maier, *Plasmonics: Fundamentals and Applications*, Springer, New York, 2007, pp. xxiv, p. 223.
11 D. K. Gramotnev and S. I. Bozhevolnyi, *Nat. Photonics*, 2010, **4**, 83–91.
12 D. R. Ward, F. Huser, F. Pauly, J. C. Cuevas and D. Natelson, *Nat. Nanotechnol.*, 2010, **5**, 732–736.
13 P. S. Davids, J. Kirsch, A. Starbuck, R. Jarecki, J. Shank and D. Peters, *Science*, 2020, **367**, 1341–1345.
14 C. W. Berry, N. Wang, M. R. Hashemi, M. Unlu and M. Jarrahi, *Nat. Commun.*, 2013, **4**, 1622.
15 Y. Y. Cai, J. G. Liu, L. J. Tauzin, D. Huang, E. Sung, H. Zhang, A. Joplin, W. S. Chang, P. Nordlander and S. Link, *ACS Nano*, 2018, **12**, 976–985.
16 Y. J. Lu, R. Sokhoyan, W. H. Cheng, G. K. Shirmanesh, A. R. Davoyan, R. A. Pala, K. Thyagarajan and H. A. Atwater, *Nat. Commun.*, 2017, **8**, 1631.
17 L. Mester, A. A. Govyadinov, S. Chen, M. Goikoetxea and R. Hillenbrand, *Nat. Commun.*, 2020, **11**, 3359.
18 I. Mehdi, J. V. Siles, C. Lee and E. Schlecht, *Proc. IEEE*, 2017, **105**, 990–1007.
19 M. Naftaly, R. G. Clarke, D. A. Humphreys and N. M. Ridler, *Proc. IEEE*, 2017, **105**, 1151–1165.
20 H. R. Zhang, Y. Y. Yu, I. Getmanov and A. Shamim, *IEEE Antenn. Propag. Mag.*, 2024, **66**, 51–64.
21 M. Tang, J. M. Alexander, D. Kwon, A. D. Estillore, O. Laskina, M. A. Young, P. D. Kleiber and V. H. Grassian, *J. Phys. Chem. A*, 2016, **120**, 4155–4166.
22 R. Chatterjee, I. M. Pavlovetc, K. Aleshire and M. Kuno, *J. Phys. Chem. C*, 2018, **122**, 16443–16463.
23 H. Hu, X. Yang, F. Zhai, D. Hu, R. Liu, K. Liu, Z. Sun and Q. Dai, *Nat. Commun.*, 2016, **7**, 12334.
24 M. Abb, Y. Wang, N. Papasimakis, C. H. de Groot and O. L. Muskens, *Nano Lett.*, 2014, **14**, 346–352.
25 K. L. Domina, V. V. Khardikov, V. Goryashko and A. Y. Nikitin, *Adv. Opt. Mater.*, 2019, **8**, 1900942.
26 F. Neubrech, D. Weber, R. Lovrincic, A. Pucci, M. Lopes, T. Toury and M. L. de la Chapelle, *Appl. Phys. Lett.*, 2008, **93**, 163105.
27 J. Chen, P. Albella, Z. Pirzadeh, P. Alonso-Gonzalez, F. Huth, S. Bonetti, V. Bonanni, J. Akerman, J. Nogues, P. Vavassori, A. Dmitriev, J. Aizpurua and R. Hillenbrand, *Small*, 2011, **7**, 2341–2347.
28 Y. Yao, M. A. Kats, R. Shankar, Y. Song, J. Kong, M. Loncar and F. Capasso, *Nano Lett.*, 2014, **14**, 214–219.
29 M. Schnell, A. Garcia-Etxarri, A. J. Huber, K. B. Crozier, A. Borisov, J. Aizpurua and R. Hillenbrand, *J. Phys. Chem. C*, 2010, **114**, 7341–7345.
30 J. Martin, M. Kociak, Z. Mahfoud, J. Proust, D. Gerard and J. Plain, *Nano Lett.*, 2014, **14**, 5517–5523.
31 T. Neuman, P. Alonso-Gonzalez, A. Garcia-Etxarri, M. Schnell, R. Hillenbrand and J. Aizpurua, *Laser Photonics Rev.*, 2015, **9**, 637–649.
32 F. J. García de Abajo, *Rev. Mod. Phys.*, 2010, **82**, 209–275.
33 A. L. Koh, A. I. Fernandez-Dominguez, D. W. McComb, S. A. Maier and J. K. Yang, *Nano Lett.*, 2011, **11**, 1323–1330.

34 M. W. Chu, V. Myroshnychenko, C. H. Chen, J. P. Deng, C. Y. Mou and F. J. Garcia de Abajo, *Nano Lett.*, 2009, **9**, 399–404.
35 D. T. Schoen, A. C. Atre, A. Garcia-Etxarri, J. A. Dionne and M. L. Brongersma, *Nano Lett.*, 2015, **15**, 120–126.
36 N. Mirsaleh-Kohan, V. Iberi, P. D. Simmons Jr, N. W. Bigelow, A. Vaschillo, M. M. Rowland, M. D. Best, S. J. Pennycook, D. J. Masiello, B. S. Guiton and J. P. Camden, *J. Phys. Chem. Lett.*, 2012, **3**, 2303–2309.
37 P. Alonso-Gonzalez, P. Albella, F. Golmar, L. Arzubiaga, F. Casanova, L. E. Hueso, J. Aizpurua and R. Hillenbrand, *Opt. Express*, 2013, **21**, 1270–1280.
38 N. W. Bigelow, A. Vaschillo, V. Iberi, J. P. Camden and D. J. Masiello, *ACS Nano*, 2012, **6**, 7497–7504.
39 D. T. Schoen, A. L. Holsteen and M. L. Brongersma, *Nat. Commun.*, 2016, **7**, 12162.
40 C. A. Balanis, *Antenna Theory: Analysis and Design*, Wiley, Hoboken, New Jersey, 4th edn, 2016, p. 1072.
41 Y. C. Xu, E. Tucker, G. Boreman, M. B. Raschke and B. A. Lail, *ACS Photonics*, 2016, **3**, 881–885.
42 C. Moreno and G. Boreman, *J. Infrared, Millimeter, Terahertz Waves*, 2021, **42**, 504–513.
43 R. Büchner, T. Weber, L. Kühner, S. A. Maier and A. Tittl, *ACS Photonics*, 2021, **8**, 3486–3494.
44 F. J. Garcia de Abajo and V. Di Giulio, *ACS Photonics*, 2021, **8**, 945–974.
45 F. J. Garcia de Abajo and M. Kociak, *Phys. Rev. Lett.*, 2008, **100**, 106804.
46 U. Hohenester, H. Ditlbacher and J. R. Krenn, *Phys. Rev. Lett.*, 2009, **103**, 106801.
47 A. Wiener, H. Duan, M. Bosman, A. P. Horsfield, J. B. Pendry, J. K. Yang, S. A. Maier and A. I. Fernandez-Dominguez, *ACS Nano*, 2013, **7**, 6287–6296.
48 A. A. Govyadinov, A. Konecna, A. Chuvilin, S. Velez, I. Dolado, A. Y. Nikitin, S. Lopatin, F. Casanova, L. E. Hueso, J. Aizpurua and R. Hillenbrand, *Nat. Commun.*, 2017, **8**, 95.
49 S. Lazar, Y. Shao, L. Gunawan, R. Nechache, A. Pignolet and G. A. Botton, *Microsc. Microanal.*, 2010, **16**, 416–424.
50 S. J. Pennycook, C. Li, M. Li, C. Tang, E. Okunishi, M. Varela, Y. M. Kim and J. H. Jang, *J. Anal. Sci. Technol.*, 2018, **9**, 11.
51 J. Park, S. Heo, J. G. Chung, H. Kim, H. Lee, K. Kim and G. S. Park, *Ultramicroscopy*, 2009, **109**, 1183–1188.
52 J. Wei, T. Ogawa, B. Feng, T. Yokoi, R. Ishikawa, A. Kuwabara, K. Matsunaga, N. Shibata and Y. Ikuhara, *Nano Lett.*, 2020, **20**, 2530–2536.
53 M. J. Lagos, A. Trugler, U. Hohenester and P. E. Batson, *Nature*, 2017, **543**, 529–532.
54 E. P. Bellido, D. Rossouw and G. A. Botton, *Microsc. Microanal.*, 2014, **20**, 767–778.
55 M. J. Lagos, I. C. Bicket, M. S. Mousavi and G. A. Botton, *Microscopy*, 2022, **71**, i174–i199.
56 A. Polman, M. Kociak and F. J. Garcia de Abajo, *Nat. Mater.*, 2019, **18**, 1158–1171.
57 D. Sarid and W. A. Challener, *Modern Introduction to Surface Plasmons : Theory, Mathematica Modeling, and Applications*, Cambridge University Press, Cambridge; New York, 2010, p. 371.
58 A. A. Kichigin and M. A. Yurkin, *J. Phys. Chem. C*, 2023, **127**, 4154–4167.
59 G. D. Bernasconi, J. Butet, V. Flauraud, D. Alexander, J. Brugger and O. J. F. Martin, *ACS Photonics*, 2016, **4**, 156–164.
60 A. Losquin and M. Kociak, *ACS Photonics*, 2015, **2**, 1619–1627.
61 V. Myroshnychenko, J. Nelayah, G. Adamo, N. Geuquet, J. Rodriguez-Fernandez, I. Pastoriza-Santos, K. F. MacDonald, L. Henrard, L. M. Liz-Marzan, N. I. Zheludev, M. Kociak and F. J. Garcia de Abajo, *Nano Lett.*, 2012, **12**, 4172–4180.
62 J. Kischkat, S. Peters, B. Gruska, M. Semtsiv, M. Chashnikova, M. Klinkmuller, O. Fedosenko, S. Machulik, A. Aleksandrova, G. Monastyrskyi, Y. Flores and W. T. Masselink, *Appl. Opt.*, 2012, **51**, 6789–6798.
63 R. L. Olmon, B. Slovick, T. W. Johnson, D. Shelton, S. H. Oh, G. D. Boreman and M. B. Raschke, *Phys. Rev. B: Condens. Matter Mater. Phys.*, 2012, **86**, 235147.
64 L. Reimer and H. Kohl, *Transmission Electron Microscopy: Physics of Image Formation*, Springer, New York, NY, 5th edn, 2008, p. 587.
65 U. Hohenester and J. R. Krenn, *Phys. Rev. B: Condens. Matter Mater. Phys.*, 2005, **72**, 195429.
66 S. Thomas, C. Matyssek, W. Hergert, M. Arnold, L. Kiewidt, M. Karamehmedovic and T. Wriedt, *Plasmonics*, 2016, **11**, 865–874.
67 Y. Cao, A. Manjavacas, N. Large and P. Nordlander, *ACS Photonics*, 2015, **2**, 369–375.
68 U. Hohenester, H. Ditlbacher and J. R. Krenn, *Phys. Rev. Lett.*, 2009, **103**, 106801.
69 E. Cubukcu and F. Capasso, *Appl. Phys. Lett.*, 2009, **95**, 201101.
70 H. W. Jia, F. Yang, Y. Zhong and H. T. Liu, *Photonics Res.*, 2016, **4**, 293–305.
71 P. Alonso-Gonzalez, P. Albella, F. Neubrech, C. Huck, J. Chen, F. Golmar, F. Casanova, L. E. Hueso, A. Pucci, J. Aizpurua and R. Hillenbrand, *Phys. Rev. Lett.*, 2013, **110**, 203902.
72 D. M. Pozar, *Microwave Engineering*, Wiley, Hoboken, NJ, 4th edn, 2012, p. 732.
73 L. Galatro and M. Spirito, *IEEE Trans. Microwave Theory Tech.*, 2017, **65**, 1315–1323.
74 M. Horibe and M. Yoshida, *2015 45th European Microwave Conference*, EuMC, 2015, 1007–1010.